Microbial metallogenesis of Cryogenian manganese ore deposits in South China

Wenchao Yu[1], Márta Polgári[2,3], Ildikó Gyollai[2], Krisztián Fintor[4], Máté Szabó[2], Ivett Kovács[2], József Fekete[2], Yuansheng Du[1,*], Qi Zhou[5]

[1] State Key Laboratory of Biogeology and Environmental Geology, School of Earth Sciences, China University of Geosciences, Wuhan 430074, China, e-mail: yuwenchaocug@163.com, duyuansheng126@126.com

[2] Research Centre for Astronomy and Geosciences, IGGR, HAS, 1112 Budapest, Budaörsi str. 45, Hungary, e-mail: rodokrozit@gmail.com, gyildi@gmail.com, szmatez@gmail.com, iv.kovacs@gmail.com, fekete.jozsef@csfk.mta.hu

[3] Eszterházy Károly University, Department of Natural Geography and Geoinformatics, 3300 Eger, Leányka str. 6, Hungary

[4] Szeged University, Dept. of Mineralogy, Geochemistry and Petrology, 6722 Szeged, Egyetem, str. 2-6, Hungary, e-mail: efkrisz@gmail.com

[5] Guizhou Bureau of Geology and Mineral Exploration and Development, Guiyang 550004, China, e-mail: 103zq@163.com

* Corresponding author: Corresponding author: duyuansheng126@126.com; Tel: +86 13971241916, Fax: +86 27 87481365.

Abstract

The Datangpo Formation manganese deposits (DFMnD) in South China formed during the interglacial stage between the Sturtian and Marinoan glaciations of the Cryogenian period. These black shale-hosted deposits are composed of massive Mn-carbonates with microscopic laminae/laminations and cherty veins. To date, it has been thought that the DFMnD formed through inorganic processes, which were controlled by redox changes in the post-Sturtian Nanhua Rift Basin, South China. However, in this study, systematic petrographic, mineralogical, and geochemical analyses indicate a microbially mediated origin of the Mn ore deposits. Mineralized microbial woven micro-textures (observed at the μm scale) and microbial fossils are common in the laminated Mn-carbonate ores. We infer that microbial enzyme activity formed poorly crystallized Mn oxide/hydroxides and carbonaceous material, which transformed to rhodochrosite, kutnohorite, ankerite/dolomite, framboidal pyrite, and apatite via diagenesis. Some micro-scale quartz and K-feldspar may be detrital but most appears to have formed during diagenesis or through hydrothermal activity. A micro-mineralogical profile determined by 2500 spectra via high-resolution *in situ* micro-Raman spectroscopy also revealed cyclic laminations of Ca-rhodochrosite as microbialite (ankerite/dolomite) and quartz, indicating a mineralized biomat system. Ca-rhodochrosite transformed to kutnohorite under elevated temperatures, as indicated by the maturation level of organic matter (determined via Raman spectroscopy). Alternating micro-laminae denote cyclic changes in microbial groups (Mn- and Fe-oxidizing microbes versus cyanobacteria) during the formation of the Mn ore deposits. Our proposed model for the microbially mediated metallogenesis of Mn-carbonate deposits begins with enzymatic multi-copper oxidase processes associated with autotrophic microbial activity under obligatory oxic conditions, which results in the precipitation of Mn bio-oxides. Following their burial in organic-rich sediments, the Mn(IV) oxides and hydroxides are reduced, producing soluble Mn(II) via processes mediated by heterotrophic microbes under suboxic conditions, which in turn form the Mn-carbonates. This microbial metallogenesis model for the Cryogenian DFMnD in South China is similar to that proposed for the Jurassic Úrkút Mn deposit in Hungary, indicating that a two-step microbially mediated process of Mn ore formation might be common throughout geological history.

Keywords: Geomicrobiology; Post-Sturtian; Datangpo; Guizhou

1. INTRODUCTION

The Cryogenian period (~720–635 Ma) experienced dramatic global climate swings between glacial and interglacial stages (Hoffman et al., 1998; Fairchild and Kennedy, 2007; Pierrehumbert et al., 2011). The Sturtian (~720–660 Ma) and Marinoan (~650–635 Ma) glaciations deposited glacial sediments worldwide, with interglacial deposits between the two that are typically marked by a basal cap carbonate and overlying clastic or carbonate deposits (Corsetti and Lorentz, 2006). Cryogenian geobiology and fossil records have sparked considerable interest in recent decades (Hoffman et al., 2017), and studies have shed light on important issues relating to the evolution of early life. Notable examples include studies on early life forms in extreme cold environments and their evolutionary significance in geological history (Ye et al., 2015; Brocks et al., 2016), as well as biotic recovery following glacial stages (Yin, 1990; Wang et al., 2008; Pruss et al., 2010; Le Ber et al., 2013).

A complete Cryogenian sequence can be found in the Nanhua Basin of the South China Craton (Dobrzinski and Bahlburg, 2007; Huang et al., 2014). Geochronological data suggest that the diamictite deposits in the Jiangkou–Chang'an (or Gucheng, Tiesi'ao) Formation and Nantuo Formation represent Sturtian and Marinoan glacial deposits, respectively (Zhou et al., 2004; Zhang et al., 2008a; Lan et al., 2014, 2015; Liu et al., 2015; Yu et al., 2017). The Cryogenian interglacial deposits in South China are collectively referred to as the Datangpo Formation, and are marked by basal Mn-carbonate ore deposits (Chen et al., 2008; Li et al., 2012; Wu et al., 2016; Yu et al., 2016). Recent studies on the Datangpo Formation indicate stepwise oxidization of seawater in the Nanhua Basin after the Sturtian glaciation (Li et al., 2012; Zhang et al., 2015; Yu et al., 2016; Ye et al., 2018). As such, it has been proposed that the Datangpo Formation Mn deposit (DFMnD) formed via an inorganic redox-controlled mechanism (Wu et al., 2016; Yu et al., 2016). Although evidence of microbial activity (e.g., fossils of microalgae, biomarker data, and framboidal pyrite) has been reported for the DFMnD, the linkage between microbes and Mn metallogenesis has long been neglected (Yin, 1990; Fan et al., 1993; Fan et al., 1999; Wang et al., 2008).

Biochemical and geobiological research has revealed the important role that microbes play in the formation of Mn minerals in sediments. New microbial pathways for the formation of Mn-rich deposits indicate that Mn fixation begins with the microbially mediated oxidation of soluble Mn(II) to solid Mn(III/IV) oxides within the sediment (Nealson et al., 1988; Mandernack et al., 1995; Tebo et al., 2004; Webb et al., 2005). Mn(IV) oxides may then be further reduced to form Mn-carbonates or Mn-silicates, also through microbially mediated processes (Thamdrup et al., 2000; Johnson et al., 2016a,b). A series of recent publications examining the participation of microbes in the genesis of selected Mn deposits ranging in age from Precambrian to Mesozoic suggest a common microbially mediated metallogenic mechanism (Fan et al., 1999; Polgári et al., 2012a, 2012b, 2016b; Biondi and Lopez, 2017; Rajabzadeh et al., 2017).

In this study, we carried out detailed micro-scale petrographic and mineralogical analyses of the Cryogenian age DFMnD, and our extensive high-resolution dataset suggests that microbial activity played a fundamental role in its metallogenesis.

2. GEOLOGICAL SETTING

The study area is located in northeastern Guizhou Province, South China (Fig. 1A). Tectonically, it belongs to the southeastern margin of the Yangtze Block, where the Nanhua Rift Basin developed after the Tonian period (Wang and Li, 2003). During the Cryogenian, the E–W-trending Nanhua Rift Basin was divided into three main paleogeographic units: the Wuling and Xuefeng Sub-rift Basins to the north and south, which were separated by the Tianzhu–Huaihua Uplift region (Zhou et al., 2016) (Fig. 1B). Cryogenian successions are found in both the sub-rift basins and uplift areas. In the Wuling Sub-rift Basin and Tianzhu–Huaihua Uplift region, the Cryogenian successions are divided into the Tiesi'ao, Datangpo, and Nantuo Formations in ascending stratigraphic order. The Tiesi'ao Formation represents the Sturtian glacial deposit and consists of >1–15 m thick, massive, dark gray diamictite or dolomitic diamictite gravels, both with poor roundness and sorting. The Datangpo Formation represents the post-Sturtian interglacial and was deposited over a ~10 Myr interval (663–654 Ma) (Zhou et al., 2004; Liu et al., 2015; Yu et al., 2017; Bao et al., 2018). It can be subdivided into three members: the first member consists of 0.5–15 m of laminated or massive Mn-carbonate and Mn-bearing shale or 2–4 m of dolomite; the second is comprised of 1–20 m of pyritic black shales; and the third member consists of 100–700 m of gray and yellow sandy or muddy siltstone (Yu et al., 2016, 2017). The Nantuo Formation represents another massive diamictite deposit with a thickness of between 60 and 200 m; U–Pb isotope ages of 654–635 Ma constrain it as a Marinoan glaciation deposit (Condon et al., 2005; Zhang et al., 2008b).

The thickness of Cryogenian successions in the Nanhua Rift Basin varies dramatically between the uplift region and sub-rift basin area (Fig. 1C). In the uplift region, the Datangpo Formation is typically <20 m thick, and lithological units are sometimes absent (e.g., the Tiesi'ao Formation, the first and second members of the Datangpo Formation) (Zhou et al., 2016). In the sub-rift basin region, the thickness of the Cryogenian succession is greater than in the uplift region and there are further differences between the successions in the grabens and horsts of the sub-rift basin. In the graben areas, "typical" Cryogenian successions are present: that is, the Tiesi'ao Formation is widely distributed and consists of diamictite, and the overlying several-hundred-meter-thick Datangpo Formation contains full Mn ore and black shale members. Conversely, recent research has revealed that in the horst areas the Tiesi'ao

Formation consists mainly of dolomitic diamictite and the first member of the Datangpo Formation lacks the Mn ore deposit, instead containing a 2–4 m thick layer of dolomitic cap carbonate (Yu et al., 2017).

3. SAMPLES

Samples from three sites were investigated in this study, including two mining tunnel sections (LB-A and LB-B) and one drill core section (ZK2001). These three sections are located in the south of Wuluo village, Songtao County, southeastern Guizhou (Fig. 2). The Datangpo Formation in the mining tunnel and drill core can be found at depths of 800–1000 m.

The Cryogenian successions at these sample sites have similar lithological features (Fig. 3). At the base of the succession, the 3–4 m thick diamictites of the Tiesi'ao Formation lie unconformably on the Tonian Qingshuijiang Formation sandstone. The overlying Datangpo Formation ranges in thickness from 209 to 391 m. The 1.2–4.6 m thick first member (Mn ore layer) of the Datangpo Formation consists mainly of laminated Mn-carbonate deposits. The Mn ore layer is overlain by the black shale (second member) and the thicker clayey siltstone (third member). The diamictite of the Nantuo Formation sits unconformably on the Datangpo Formation. A representative sample LB-171 was collected from the boundary between the Mn ore deposit and the overlying black shale in mining tunnel LB-A. Representative samples LB-304 and ZK2001-183 were collected from the laminated Mn ore layer in mining tunnel LB-B and drill core ZK2001 (Fig. 3).

Covered thin sections were made from laminated Mn ore samples LB-304 and ZK2001-83, and black shale sample LB-171 for examination via optical microscopy (OM) (Fig. 4). A piece of laminated Mn carbonate ore (LB-304-Mn-ore) was examined for bulk X-ray diffraction (XRD), and a thin section (HU-LB-304) of this rock sample was used for optical rock microscopy, Raman spectroscopy, X-ray fluorescence (XRF), Fourier-transform infrared spectroscopy (FTIR), cathodoluminescence (CL), and scanning electron microscope energy dispersive X-ray spectroscopy (SEM-EDS) studies.

4. METHODS

4.1. Optical rock microscopy (OM)

Petrographic structural-textural studies were made on four thin section in transmitted light (NIKON SMZ800 microscope and NIKON ECLIPSE 600 rock microscope in the Institute for Geological and Geochemical Research, Research Centre for Astronomy and Earth Sciences, Hungarian Academy of Sciences (IGGR RCAES HAS, Budapest, Hungary). In total, 96 photos and panorama photo series of all thin sections were taken.

4.2. Cathodoluminescence microscopy (CL)

Cathodoluminescence (CL) petrography was carried out on 1 thin section and an ore slice using a Reliotron cold cathode cathodoluminescence apparatus mounted on a BX-43 Olympus polarization microscope (Szeged University, Hungary). Accelerating voltage was 7-7.7 keV during the analysis. Cathodoluminescence spectra were recorded by using an Ocean Optics USB2000+VIS-NIR spectrometer. Spectrometer specifications are 350-1000 nm wavelength range, and 1.5 nm (FWHM) optical resolution. Interpretation was made according to Marshall (1998).

4.3. X-Ray powder diffraction (XRD)

Mineralogical analyses were performed on 1 bulk sample (LB-304) using a Rigaku Miniflex-600 X-ray diffractometer (XRD), with carbon monochromator and Cu-Kα radiation, at 40 kV and 15 mA (IGGR RCAES HAS, Budapest, Hungary). Mineral composition was determined on randomly oriented powdered samples. The diffraction patterns were processed using Siroquant V4 software, and the modal contents were determined by the Rietveld method.

4.4. FTIR-ATR

Fourier transform infrared spectrometer (FTIR) was used for *in situ* micro-mineralogy and organic material identification on one thin section (55 spectra were taken at 12 measuring points, IGGR RCAES HAS, Budapest, Hungary), using a Bruker FTIR VERTEX 70 equipped with a Bruker HYPERION 2000 microscope with a 20x ATR objective and MCT-A detector. During attenuated total reflectance Fourier transform infrared spectroscopy (ATR) analysis, the samples were contacted with a Ge crystal (0.5 micron) tip with 1 N pressure. The measurement was conducted for 32 seconds in the 600–4000 cm^{-1} range with 4 cm^{-1} resolution. Opus 5.5 software was used to evaluate the data. The equipment cannot be used for Mn-oxide determination because those peaks fall in the <600 cm^{-1} range. Contamination by epoxy glue and glass were taken into consideration.

4.5. Raman spectroscopy

Raman spectroscopy is a very efficient and sensitive method to determine the mineralogical and organic matter compositions and distributions in the sample, which are important for genetic interpretations (Larsson and Rand, 1973; Orange et al., 1996; Chen et al., 2007; Jehlička et al., 2009; Okolo et al., 2015). High resolution *in situ* micro-Raman spectroscopy was used for micro-mineralogy and organic matter identification and distribution on 1 thin section (HU-LB-304), resulting in 2500 spectra (Szeged University, Hungary). A Thermo Scientific DXR Raman Microscope was used, with a 532 nm (green) diode pumped solid-state (DPSS) Nd-YAG laser using 2.0 mW laser power, 50x objective lens in confocal mode (confocal aperture 50 μm pinhole). Acquisition time was 30 sec and spectral resolution was ~2 cm^{-1} at each measurement; the distance between each point was 10 μm. A composite image of thin sections of Raman microscopy measurements and series of Raman spectra acquired along the vertical sections is indicated on thin section photos (arrow points to measurement direction). Diagrams were organized on peak height versus analytical spot number of each of the phases along the Raman scanned section. Intensities were normalized to the highest peak for each spectra. The following Raman bands were used for normalization: rhodochrosite: ~1086 cm^{-1}, kutnohorite: ~1083 cm^{-1}, ankerite/dolomite: ~1093-96 cm^{-1}, apatite: ~965 cm^{-1}, quartz: ~463 cm^{-1}; carbonaceous matter: ~1605 cm^{-1}. Identification of minerals was made with the RRUFF Database (Database of Raman-spectroscopy, X-ray diffraction, and chemistry of minerals: http://rruff.info/). Contamination by epoxy glue was taken into consideration. The sensitivity of FTIR is better than that of Raman spectroscopy for organic matter.

4.6. EPMA-EDS

Element composition and microtextural features of one thin section (HU-LB-304) were determined at 1-2 μm spatial resolution on a carbon-coated sample using a JEOL Superprobe 733 electron microprobe with an INCA Energy 200 Oxford Instrument Energy Dispersive Spectrometer, run at 20 keV acceleration voltage, 6 nA beam current and count time of 60 s for the spot measurement and 5 min for line-scan analysis. Olivine, albite, plagioclase and wollastonite standards were used; we estimated that the detection limit for the main elements was below 0.5% based on earlier measurements with various samples (IGGR RCAES HAS, Budapest, Hungary). 180 spectra were aquired, and 26 back scattered electron images were made.

4.7. Energy dispersive (EDS) X-ray fluorescence analysis (XRF)

Energy dispersive (EDS) X-ray fluorescence analyses were made on thin section by Horiba Jobin Yvon XGT 5000 X-ray fluorescence microscope (Szeged University, Hungary). Measurement conditions were 50 kV beam voltage, 0.1 mA beam current, and 10 μm beam spot diamater. Every single analyzed area was 1 mm * 5.124 mm along a line (longer side of the analyzed area were parallel with the line in each case) perpendicular to the lamination of the sample. Analyzed areas were divided into 512 * 100 pixels with 0.01 mm^2 size of each pixel. Intensity of each element was measured in counts per second (cps).

5. RESULTS

5.1. Optical microscopy (OM)

Textural observations of the thin sections reveal mineralized biomats (Fig. 4), which are clearly visible in the lower magnification OM images. The thin sections of the laminated Mn ore and black shale show very similar features. OM examination of all the thin sections at high resolution (×1000) reveals a series of biomat microstructures as the main constituents (Fig. 5). These microstructures are filamentous, and have bead-like, or coccoid forms, and the fabrics of the entire samples are densely woven.

In the thin section of HU-LB-304, segregated quartz precipitates are generally widespread and associated with very fine-grained carbonates. These mostly follow the original lamination of the sample, partially cross-cutting it in places (Fig. 4H). The quartz and carbonate are often found to be mixed on a very small scale. Although laminations are observed in the thin section, detrital interbedding is not observed. The fine-grained matrix consists of carbonate (Ca-rhodochrosite, kutnohorite, and ankerite), with additional organic matter, apatite, pyrite, and quartz. Rhodochrosite, kutnohorite, and quartz were also detected by XRD. In the middle part of the thin section (HU-LB-304), quartz-rich laminae consisting more or less rhodochrosite are present. The elongated fibrous microstructure of the quartz crystals is characteristic of precipitation from a fluid that percolated across a laminated rock during a process involving hydrodynamic diffusion (Fig. 4H) (Bons, 2000; Bons et al., 2012).

5.2. Cathodoluminescence (CL)

In CL images (Fig. 6), the fine-grained rhodochrosite (mixed carbonate) gives a dull reddish (orange) luminescence color and has the appearance of compact carbonate (ore) “blocks” or lenses (“birds eye”). However, small differences in CL may reflect transitional carbonate mineral phases. The CL of the segregated quartz is not clear as the mixed carbonate (the ore phase) dominates. Late diagenetic or younger carbonate and quartz vein fillings are clearly visible.

The numerous small and large bright yellow mineral grains are apatite, and often have a paler margin (Fig. 6E, F). The spectra taken from the drill core sample support the idea of REE (Tm^{3+}?, Dy^{3+}, Sm^{3+}, Eu^{3+}, Nd^{3+}) and probably Mn^{2+} as activator elements. Thus, the paler CL color seen at the margins of the apatite grains is probably caused by the activation of Mn^{2+} ions. The apatite grains occur along the ore lenses and laminae in a woven fine-grained matrix, which mark the grain borders as accompanying series of minerals. Detrital grains (quartz clasts, feldspar, and lithic fragments) are not shown to be dominant constituents in the CL images.

CL examination of a rock slice also shows dull reddish orange carbonate luminescence, and the apatite minerals clearly follow the same woven structure. A dull lilac luminescence color marks the presence of quartz (Fig. 6E, F) and the orange vein filling is probably diagenetic kutnohorite (Polgári et al., 2007).

5.3. FTIR

A total of 55 FTIR spectra were produced from 12 positions within thin section HU-LB-304. FTIR confirms the presence of carbonate (rhodochrosite, kutnohorite, and siderite), quartz, apatite, feldspar, pyrite, ferrihydrite, lepidocrocite, hematite, and various types of organic matter (aliphatic carbon–hydrogen bound) (Madejova and Komádel, 2001; Parikh and Chorover, 2006; Polgári et al., 2007; Glotch and Rossman, 2009; Beasley et al., 2014; Müller et al., 2014) (Table S1). As stated above, both OM and CL observations indicate that the sample is very fine-grained with no obvious detrital minerals. The detection of feldspar in the FTIR spectra indicates that it occurs as a very fine-grained component in the laminated Mn ore; it has low intensity and wider peaks suggesting an authigenic origin. Pyritiferous parts are clearly visible and have a yellowish color. Ferrihydrite occurs in the vicinity of pyrite.

5.4. EPMA-EDS

The micro-scale lamination and woven biomat-like texture is clearly visible in Fig. 7 and SI 1 (HU-LB-304) and the minerals are very fine-grained and mixed. Some apatite grains reach a few tens of μm in size and pyrite grains (commonly framboidal) appear to follow the woven laminae. The light gray parts consist of a mixture of Ca-rhodochrosite and kutnohorite and also probably contain ankerite. The darker woven laminae consist of K-feldspar, quartz, and illite, and are very fine-grained (5–30 μm), which appears to exclude a detrital origin; these minerals are probably diagenetic products of extracellular polymeric substances (Dupraz and Visscher, 2005; Gyollai et al., 2015, 2017). In particular, structures that are very similar to those found in the microbial fossil record (see Polgári et al., 2012 a,b) were observed in the light gray parts (Fig. 7D). The preliminary results for the proposed mineralogy at the points on the photographs are shown in SI 1 and the chemical composition (in wt.%) is presented in Table S2. It is clear that in many cases the measurements were made on a mixture of different minerals due to the very fine grain size. The composition of Ca-rhodochrosite and kutnohorite is very variable. Mg is a prevailing accompanying element, and Fe occurs frequently.

5.5. Raman spectroscopy

The 2500 spectra were examined for their micro-mineralogical and organic matter compositions and mineral distribution along the thin section profile (Fig. 8A). The mineral distributions were evaluated visually, based on a series of Raman profiles using a 10 μm scale (SI 2). Rhodochrosite, kutnohorite, ankerite/dolomite, quartz, pyrite, apatite, feldspar, and carbonaceous material were detected (SI 2).

The cyclicity of the organic material cannot be determined based on the first 500 spectra. The organic matter consists mainly of kerogen, bound to carbonates. Manganite (the trace of a proto-Mn-oxide phase) is rare in the spectra. Hematite is present and may represent a remnant of Fe-biomats, as observed in the microscope images, where it forms a brown filamentous micro-texture (Fig. 5).

We investigated the thickness and microstructure of the laminae; the number of peaks per 1 mm section is summarized in Table S3A–B and Fig. 8 along with calculated lamina thickness. The zigzag pattern in the mineral distribution reveals cyclicity in the mineral formation; when biofilms mineralized they transformed to microbialite, which is a series of mineral laminae for now with a given few tens of cm thickness (SI 2 and 3). The average thickness of a peak (microlamina) is 24 μm, the minimum is 18 μm, and the maximum is 48 μm. Ca-rhodochrosite laminae show a peak thickness of 20–30 μm and 14–38 peaks occur in every 1 mm interval. Kutnohorite laminae show a peak thickness of 20–30 μm and 1–34 peaks occur in every 1 mm interval. Quartz laminae have a peak thickness of 20–30 μm and peaks of quartz can merge into thicker layers. Pyrite, apatite, and feldspar occur randomly, while carbonaceous material is constantly present. The peaks of Ca-rhodochrosite, kutnohorite, and ankerite show no sign of overlapping; they alternate with each other, indicating that ankerite (Fe-bearing phase) is an independent phase. For better visibility, the overlapped positions of Ca-rhodochrosite + kutnohorite, Ca-rhodochrosite + ankerite/dolomite, Ca-rhodochrosite + quartz, and Ca-rhodochrosite + kutnohorite + quartz are presented in SI 3. Ca-rhodochrosite and kutnohorite represent one system, with overlapping of the two mineral phases occurring in the entire micro-laminae system. Quartz also forms microlaminae. XRF was used to generate a profile of chemical composition parallel to the Raman trace. As the elements belong to different mineral phases of variable composition, the data are supplemental (SI 2).

The Raman carbonaceous material geothermometer using peak width was applied to the first part of the thin section, based on the method of Kouketsu et al. (2014) (Fig. 9). This demonstrated that the highest temperatures (T_{max}) reached during the thermal evolution history of the DFMnD were in the range 250–330 ºC.

6. DISCUSSION

6.1. Microbial metallogenesis of the DFMnD

6.1.1. Sediment accumulation stage of the Mn ore deposit

During the Sturtian glaciation, the Nanhua Rift Basin was highly restricted and anoxic due to the presence of the marginal barrier of the rift basin and globally low sea-levels (Li et al., 2012; Zhang et al., 2015). After the deglaciation, the development of an oxic surface water mass, as well as inputs of nutrients from the open sea and terrestrial weathering products led to the recovery of marine microbe communities. The idea of enhanced microbial activity and higher primary productivity in the post-Sturtian Nanhua Rift Basin is supported by several lines of evidence: (a) high TOC contents (1.4%–3.5%) in the post-glacial Mn ore and black shale deposits (Yu et al., 2016); (b) positive shifts in $\delta^{13}C_{carb}$ records from the post-Sturtian cap carbonate deposits (Yu et al., 2017); and (c) the microbial fossils, biomarker data, and microbially produced micro-texture (MMPT) of the minerals (Yin, 1990; Tang and Liu, 1999; Wang et al., 2008 and this study). Based on these findings, we assume that the sediment surface in the post-Sturtian Nanhua Rift Basin was densely colonized by microbes and that this was probably a common scenario in the post-Sturtian oceans worldwide (Pruss et al., 2010; Bosak et al., 2011; Le Ber et al., 2013, 2015). Because clay-sized terrigenous detrital particles were only detected by FTIR, SEM, and Raman spectroscopy, we suggest that the terrigenous input was limited during the formation of the laminated Mn ore deposits. This limited input is probably due to the fact that: (a) the study area was in the central region of the graben in the Wuling Sub-rift Basin where minimal terrigenous materials reached; (b) the first member (Mn ore deposit) and the second member (black shale) of the Datangpo Formation represent deposits formed during marine transgressions with very low sedimentation rates (<3 cm/kyr; Bao et al., 2018).

Previous work has emphasized that changes in redox conditions in the marine environment were the key factor governing the formation of the Cryogenian Mn ore deposit in the Nanhua Basin (Wu et al., 2016; Yu et al., 2016). In the post-glacial episodic ventilation model, the anoxic Nanhua Basin accumulated abundant dissolved hydrothermally derived Mn(II) during the Sturtian glaciation. When glaciation ended and a redox-stratified water column developed in the basin with an oxic surface layer and an anoxic deep layer, the accumulated dissolved Mn(II) was oxidized and precipitated as Mn-oxides on the basin floor during the episodic input of oxic bottom water. Yu et al. (2016) hypothesized that Mn(II) enzymatic oxidation was a possible mechanism for the fixation of dissolved Mn(II), but without any solid evidence. In this study, the microbe fossils, interwoven textures, and micro-scale Ca-rhodochrosite + kutnohorite laminations preserved in the Mn ore samples as microbialites, all indicate that the micro-scale laminations were generated by microbial activity (biomat system) during the formation of the Mn-carbonate ore deposits of the DFMnD.

Microbially mediated Mn fixation has been considered an important mechanism for Mn enrichment in sediments. Diem and Stumm (1984) reported that even in the presence of relatively high oxygen levels, Mn did not precipitate from sterile solutions, implying the need for catalysis. Such catalytic reactions have, for instance, been observed on the surfaces of dormant bacterial spores (Nealson and Tebo, 1980; Rosson and Nealson, 1982) or in association with exopolymers (extracellular oxidation; Ghiorse, 1986). After the Sturtian glaciation, recovery of the microbes in the Nanhua Rift Basin activated the Mn cycle between the seawater and sediments (Johnson et al., 2016b). Two kinds of microbial groups, Mn-oxidizing microbes and cyanobacteria, led the Mn enrichment process during this period. The enzymatic Mn(II) oxidation conducted by Mn-oxidizing microbes resulted in the accumulation of δ-MnO_2 bio-oxide as very fine-grained ooze within the cyanobacterial organic network (e.g., extracellular polymeric substance or EPS; Table 1; Fig. 10A). This process sequestered Mn(II) from solution to the solid phase and was accompanied by microbially mediated Mg enrichment (Havig et al., 2015). There was no evidence for the formation of authigenic clay minerals or other minerals, but considerable amounts of microbial organic matter had clearly accumulated in this stage. Cyanobacterial activity also recovered in the post-Sturtian Nanhua Rift Basin, as shown by biomarker (Wang et al., 2008) and carbon isotope evidence (Yu et al., 2017). Bioessential elements, including Ca, Si, and P, were enriched in the cyanobacterial system through binding of these elements and clay-sized detritus with EPS (Dupraz and Visscher, 2005; Dupraz et al., 2009). Cyanobacteria and Mn-oxidizing microbes have their own cyclic activities (probably day/night in the case of cyanobacteria) and these two cycles existed in one space on the surface of sediments (Fig. 10A). The presence of ferrihydrite in the Mn ore sample indicates that the Fe(II)-oxidizing microbes occasional formed weak Fe-biomats.

6.1.2. Post-burial diagenesis of the Mn ore deposits

In the early stages of diagenesis, both cyanobacterial and microbial Mn activity occurred, and a series of Mn- or Fe-bearing carbonates formed (Table 1; Fig. 10 B, C). The EPS network present during diagenesis occupied the space until the respective diagenetic minerals formed. Microbially mediated reactions between δ-MnO_2 bio-oxide and organic matter were mainly responsible for the formation of the

Mn-carbonate deposits (Roy, 2006; Maynard, 2014; Johnson et al., 2016b). This mechanism also resulted in the negative $\delta^{13}C$ signals preserved in the DFMnD ($\delta^{13}C_{carb}$ = –5‰ to –9‰ and $\delta^{13}C_{org}$ = –30‰ to –33‰, Chen et al., 2008; Yu et al., 2017). Some of the organic matter became mineralized as carbonates. At the same time, the decomposition of cyanobacterial cells and EPS began, which liberated Ca, Si, P, and other elements firmly related to microbial activity (e.g., K and Al). The formation of Mn-bearing calcite can proceed along multiple paths. The most common explanation is that Ca^{2+} attaches to pre-existing rhodochrosite and substitutes for a fraction of the Mn (Maynard, 2014). The formation of kutnohorite is peculiar, as this is a rare mineral and not a syngenetic sedimentary one. It is likely that elevated temperatures created favorable conditions for its formation as supported by the Raman carbonaceous material geothermometer (~300 °C in Fig. 9B) (Žák and Povondra, 1981; Polgári et al., 2007). The lamination of ankerite is not as regular as that in rhodochrosite and kutnohorite. The distribution of ankerite was possibly controlled by that of scattered Fe-biomats during the sedimentary stage.

The formation of some important accessory minerals in the DFMnD also appears to be linked to diagenetic processes. Fine quartz laminae probably formed from mobilized silicon after the decomposition of cyanobacterial cells, as living cyanobacteria collect silica on their surface to form endo- or exoskeletons (Yee et al., 2003; Dupraz et al., 2009). In the same way, the liberated P and Ca led to the formation of apatite (through the recrystallization of fine-grained phosphorite, whose distribution can be clearly seen in the CL photos (Fig. 6F–H). During diagenesis, the system became anoxic and framboidal pyrite formed through bacterial sulfate reduction (BSR) in the sulfate reduction zone. Although the pyrite framboids in the DFMnD range from 10 to 30 μm in size, previous research has revealed that the pyrite framboids in the DFMnD witnessed thermochemical sulfate reduction (TSR) and contain growth rims with superheavy $\delta^{34}S_{pyrite}$ (+50‰ to +70‰) and normal cores with biogenic $\delta^{34}S_{pyrite}$ values (+15‰ to +20‰) (Cui et al., 2018). The original diameters of the pyrite framboids in the DFMnD should have been 2–5 μm. Formerly, feldspar was thought to have a detrital origin, similar to quartz, but our FTIR and SEM-EDS results suggest it most probably has a diagenetic origin. K and Na can be liberated via the decomposition of cell and EPS to participate in the formation of feldspar together with the segregating silica; such authigenic feldspar shows no luminescence, which would support a diagenetic origin for the DFMnD feldspars (Marshall, 1998). Clay minerals (illite) were only observed on a micro-scale and are also diagenetic products. The DFMnD was not dominated by clay mineralization (Polgári et al., 2012a, 2012b) unlike other black shale-hosted Mn-carbonate deposits (e.g., the Jurassic Úrkút Mn-carbonate deposit in Hungary). Possible explanations for the limited clay mineral content in the DFMnD are as follows:

(1) Detrital clay minerals were rare (or not dominant) because ore bed formation occurred in the center of a basin where terrestrial inputs were minimal;

(2) Diagenetic clay mineral formation did not become a dominant contributor to mineralogical composition because: i) the liberation of ions was not synchronous, and if Ca^{2+} mobilized first it could be incorporated into existing carbonates with the later mobilized silica possibly forming quartz; ii) if silica dissolved first, the other ions were missing for clay formation and quartz formed instead; iii) conditions were not favorable at all for clay mineral formation.

6.2. Comparison of the Cryogenian DFMnD in South China with the Jurassic Úrkút Mn deposit in Hungary

The Early Jurassic (Toarcian) Úrkút Mn deposit in Hungary contains strong evidence for microbially mediated metallogenesis in a two-step microbially mediated Mn ore formation model. Located in the central Bakony Mountains, the North Pannonian unit of the Alps–Carpathians–Pannonian region, the Úrkút Mn deposit also formed in a graben, in this case in the failed rift basin that accompanied the spreading of the Neotethys Ocean and Alpine Tethys (Haas, 2012; Polgári et al., 2012b). As one of the most important giant Mn ore deposits in central Europe, reserves of the Úrkút Mn deposit amount to nearly 300 million tons (Mt) (Polgári et al., 2017). The Mn ore is preserved in two main laminated Mn-carbonate layers within a black shale sequence: a 8–12 m thick lower layer and a 2–4 m thick upper layer (Polgári et al., 2012b). The mineralogical composition of the Mn ore is dominated by Mn-carbonate (Ca-rhodochrosite and kutnohorite) along with Fe minerals (goethite, pyrite, celadonite, and Fe-smectite). Mn ore beds are separated by the black shale host (Polgári et al., 2013, 2016a). The entire ore bed is composed of millimeter-scale woven structures with widespread microbe fossils, indicating a biogenetic origin for the Mn-carbonate deposit, and both Mn and Fe are initially enriched in the biomats (Polgári et al., 2007, 2012a,b, 2013, 2016a,b).

There are therefore some important similarities between the Cryogenian DFMnD in South China and Jurassic Úrkút Mn deposit in Hungary. Thus, a scenario for their formation was presented by Polgári et al. (2012a) based on the following points:

(1) Both Mn deposits were formed in the grabens of rift basins with relatively deep and redox-stratified water conditions, where metal ions (Mn^{2+} and Fe^{2+}) originated from hydrothermal/exhalative sources at the bottom of the basins (Haas, 2012; Yu et al., 2016, 2017).

(2) Accumulation of initial Mn-oxides in both areas occurred under oxic conditions; indeed, Mn enrichment itself serves as an indicator for obligatory oxic conditions in the geological record (Maynard, 2010; Johnson et al., 2016b). Changes in oxygen supply determined whether Mn ores (the enzymatic Mn oxidation engine starts under obligatory oxic conditions) or black shales (formed under slightly decreasing oxygen supply) accumulated in both the post-Sturtian Nanhua Basin (Zhang et al., 2015; Yu et al., 2016) and the Early Jurassic Úrkút Basin (Polgári et al., 2012a, 2016a). The oxic and low temperature (<100˚C) aquatic systems would have favored microbially mediated Mn(II) oxidation in both locations (Tebo et al., 2004; Tang et al., 2013).

(3) Evidence for the two-step microbially mediated Mn-carbonate formation is similar in the two Mn deposits. A prevailing oxygen supply during the deposition of both deposits is generally reflected in mineralized microbial structures (microlamination, microtextural evidence such as woven textures, and the presence of biomats as detected by Raman profiles) and particularly supported by (i) cyanobacterial activity and microbiogenic Mn micro-laminae with embedded organic material in the DFMnD and (ii) microbiogenic Mn-rich micro-laminae, a series of Fe-biomats, celadonite, and embedded organic material in the Úrkút Mn deposits.

The results of our study are extrapolated to the level of ore formation and, although this will be different between comparable ore deposits (differences between the two Mn deposits are summarized in Table 2; e.g., Fe content), the basic process of Mn enrichment is the same. Thus, despite the large temporal gap between the two Mn deposits (Cryogenian vs. Jurassic; ~480 Myr), the overall microbial mechanism for Mn biomineralisation/metallogenesis remained the same.

6. CONCLUSIONS

(1) The Cryogenian DFMnD in Guizhou, South China, contains micro-scale evidence for biogenic influence on Mn metallogenesis. Microbial woven micro-

textures, microbial fossils, and pyrite framboids are prevalent in the laminated Mn-carbonate ore samples. High-resolution *in situ* micro-Raman spectroscopy reveals variations in the mineralogy (Ca-rhodochrosite, kutnohorite, ankerite/dolomite, and quartz) of the microlaminae. This potentially indicates changes in the microbial assemblage (Mn- and Fe-oxidizing microbes and cyanobacteria) during the formation of the Mn ore deposits resulting in mineralized laminae (microbialite) with alternating compositions.

(2) A model for the two-step microbially mediated Mn-carbonate formation of the DFMnD is proposed based on new evidence. Precipitation of Mn started by the activation of the enzymatic multi-copper oxidase process via autotrophic microbial activity under oxic conditions. After burial in organic-rich sediments, Mn(IV) oxides or hydroxides were reduced to soluble Mn(II) through processes mediated by heterotrophic microbes under sub-oxic conditions and then re-mineralized to form Mn-carbonates. Locally, the system reached the anoxic sulfate reduction zone (framboidal pyrite).

(3) A comparison of the Cryogenian DFMnD in South China and the Jurassic Úrkút Mn deposit in Hungary reveals important similarities in the formation of these Mn deposits. Thus, microbially mediated Mn-carbonate formation is a basic process in the Mn cycle that can be observed throughout the geological record.

ACKNOWLEDGMENTS

This study was supported by the Project of the Karstic Science Research Center (NSFC), Fundamental Research Funds for the Central Universities, China University of Geosciences (Wuhan) CUG170684, China Geological Survey (CGS) Project DD20160346, Guizhou Science Innovation Team Project No. 2018-5618, Research Project of Guizhou Bureau of Geology and Mineral Exploration and Development (2016-No.30). Hungarian co-authors were supported by the National Research, Development and Innovation Office, National Scientific Research Fund Hungary No. 125060, the Support of Excellence of Research Centre for Astronomy and Earth Sciences, Hungarian Academy of Sciences. Comments of Associate Editor Prof. Xianhua Li and two anonymous reviewers are highly appreciated.

References

Bao, X., Zhang, S., Jiang, G., Wu, H., Li, H., Wang, X., An, Z., Yang, T., 2018. Cyclostratigraphic constraints on the duration of the Datangpo Formation and the onset age of the Nantuo (Marinoan) glaciation in South China. Earth and Planetary Science Letters 483, 52-63.

Beasley, M.M., Bartelink, E.J., Taylor, L., Miller, R.M., 2014. Comparison of transmission FTIR, ATR, and DRIFT spectra: implications for assessment of bone bioapatite diagenesis. J Archaeol Sci 46, 16-22.

Biondi, J.C., Lopez, M., 2017. Urucum Neoproterozoic–Cambrian manganese deposits (MS, Brazil): Biogenic participation in the ore genesis, geology, geochemistry, and depositional environment. Ore Geology Reviews 91, 335-386.

Bons, P.D., 2000. The formation of veins and their micostructures. Journal of the Virtual Explorer 2.

Bons, P.D., Elburg, M.A., Gomez-Rivas, E., 2012. A review of the formation of tectonic veins and their microstructures. JSG 43, 33-62.

Bosak, T., Lahr, D.J.G., Pruss, S.B., Macdonald, F.A., Dalton, L., Matys, E., 2011. Agglutinated tests in post-Sturtian cap carbonates of Namibia and Mongolia. Earth and Planetary Science Letters 308, 29-40.

Brocks, J.J., Jarrett, A.J., Sirantoine, E., Kenig, F., Moczydłowska, M., Porter, S., Hope, J., 2016. Early sponges and toxic protists: possible sources of cryostane, an age diagnostic biomarker antedating Sturtian Snowball Earth. Geobiology 14, 129-149.

Chen, K., Leona, M., Vo-Dinh, T., 2007. Surface-enhanced Raman scattering for identification of organic pigments and dyes in works of art and cultural heritage material. SeRv 27, 109-120.

Chen, X., Li, D., Ling, H.-F., Jiang, S.-Y., 2008. Carbon and sulfur isotopic compositions of basal Datangpo Formation, northeastern Guizhou, South China: Implications for depositional environment. Progr Nat Sci 18, 421-429.

Condon, D., Zhu, M., Bowring, S., Wang, W., Yang, A., Jin, Y., 2005. U-Pb ages from the neoproterozoic Doushantuo Formation, China. Science 308, 95-98.

Corsetti, F.A., Lorentz, N.J., 2006. On Neoproterozoic cap carbonates as chronostratigraphic markers, Neoproterozoic Geobiology and Paleobiology. Springer, pp. 273-294.

Cui H., Kitajima K., Spicuzza, M. J., Fournelle, J.H., Denny A., Ishida A., Zhang F., Valley J. W., 2018. Questioning the biogenicity of Neoproterozoic superheavy pyrite by SIMS. American Mineralogist, 103 (9): 1362-1400.

Diem, D. and Stumm, W., 1984. Is dissolved Mn2+ being oxidized by O2 in absence of Mn-bacteria or Surface Catalysts? Geochim. et Cosmochim. Acta, 48: l57l-1573.Dobrzinski, N., Bahlburg, H., 2007. Sedimentology and environmental significance of the Cryogenian successions of the Yangtze platform, South China block. Palaeogeography, Palaeoclimatology, Palaeoecology 254, 100-122.

Dupraz, C., Reid, R.P., Braissant, O., Decho, A.W., Norman, R.S., Visscher, P.T., 2009. Processes of carbonate precipitation in modern microbial mats. Earth-Science Reviews 96, 141-162.

Dupraz, C., Visscher, P.T., 2005. Microbial lithification in marine stromatolites and hypersaline mats. Trends Microbiol. 13, 429-438.

Fairchild, I.J., Kennedy, M.J., 2007. Neoproterozoic glaciation in the Earth System. Journal of the Geological Society 164, 895-921.

Fan, D., Liu, T., Yang, P., Ye, J., 1993. Occurrence of Anthraxolite (Bitumen) Spheroids in Xiangtan-Type Manganese Carbonate Deposits of South China, in: Parnell, J., Kucha, H., Landais, P. (Eds.), Bitumens in Ore Deposits. Springer Berlin Heidelberg, pp. 447-458.

Fan, D., Ye, J., Yin, L., Zhang, R., 1999. Microbial processes in the formation of the Sinian Gaoyan manganese carbonate ore, Sichuan Province, China. Ore Geology Reviews 15, 79-93.

Ghiorse, W.C., 1986. Applicability of ferromanganese-depositing microorganisms to industrial metal recovery processes. Biotechnol. Bioeng. Symp., 16: 141-148.

Glotch, T.D., Rossman, G.R., 2009. Mid-infrared reflectance spectra and optical constants of six iron oxide/oxyhydroxide phases. Icar 204, 663-671.

Gyollai, I., Polgári, M. P., Fintor, K., Popp, F., Mader, D., & Pál-Molnár, E. (2015) Microbially mediated deposition of postglacial transition layers from the Neoproterozoic Otavi Group, Namibia: evidence of rapid deglaciation after the Sturtian cryogenic period. Carpathian Journal of Earth and Environmental Sciences, 10(1):63-76.

Gyollai, I., Polgari, M., Fintor, K., Pal-Molnar, E., Popp, F., & Koeberl, C. (2017) Microbial activity records in Marinoan Snowball Earth postglacial transition layers connecting diamictite with cap carbonate (Otavi Group, NW-Namibia). Austrian Journal of Earth Sciences, 110(1): 2-18.

Haas, J., 2012. Influence of global, regional, and local factors on the genesis of the Jurassic manganese ore formation in the Transdanubian Range, Hungary. Ore Geology Reviews 47, 77-86.

Havig, J.R., McCormick, M.L., Hamilton, T.L., Kump, L.R., 2015. The behavior of biologically important trace elements across the oxic/euxinic transition of meromictic Fayetteville Green Lake, New York, USA. Geochimica et Cosmochimica Acta 165, 389-406.

Hoffman, P.F., Abbot, D.S., Ashkenazy, Y., Benn, D.I., Brocks, J.J., Cohen, P.A., Cox, G.M., Creveling, J.R., Donnadieu, Y., Erwin, D.H., 2017. Snowball Earth climate dynamics and Cryogenian geology-geobiology. Sci Adv 3, e1600983.

Hoffman, P.F., Kaufman, A.J., Halverson, G.P., Schrag, D.P., 1998. A Neoproterozoic snowball earth. Science 281, 1342-1346.

Huang, J., Feng, L., Lu, D., Zhang, Q., Sun, T., Chu, X., 2014. Multiple climate cooling prior to Sturtian glaciations: Evidence from chemical index of alteration of sediments in South China. Scientific reports 4, 6868

Jehlička, J., Vítek, P., Edwards, H.G.M., 2009. Fast nondestructive Raman spectroscopic detection of minerals and biomolecules for exobiological studies. Geochmica Et Cosmochimica Acta 73.

Johnson, J.E., Savalia, P., Davis, R., Kocar, B.D., Webb, S.M., Nealson, K.H., Fischer, W.W., 2016a. Real-time manganese phase dynamics during biological and abiotic manganese oxide reduction. Environ Sci Technol 50, 4248-4258.

Johnson, J.E., Webb, S.M., Ma, C., Fischer, W.W., 2016b. Manganese mineralogy and diagenesis in the sedimentary rock record. Geochimica et Cosmochimica Acta 173, 210-231.

Kouketsu, Y., Mizukami, T., Mori, H., Endo, S., Aoya, M., Hara, H., Nakamura, D., Wallis, S., 2014. A new approach to develop the Raman carbonaceous material geothermometer for low-grade metamorphism using peak width. Isl Arc 23, 33-50.

Lan, Z., Li, X.-H., Zhang, Q., Li, Q.-L., 2015. Global synchronous initiation of the 2nd episode of Sturtian glaciation: SIMS zircon U–Pb and O isotope evidence from the Jiangkou Group, South China. Precambrian Research 267, 28-38.

Lan, Z., Li, X., Zhu, M., Chen, Z.-Q., Zhang, Q., Li, Q., Lu, D., Liu, Y., Tang, G., 2014. A rapid and synchronous initiation of the wide spread Cryogenian glaciations. Precambrian Research 255, Part 1, 401-411.

Larsson, K., Rand, R.P., 1973. Detection of changes in the environment of hydrocarbon chains by Raman spectroscopy and its application to lipid-protein systems. Biochimica et Biophysica Acta (BBA) - Lipids and Lipid Metabolism 326, 245-255.

Le Ber, E., Le Heron, D.P., Oxtoby, N.H., 2015. Influence of microbial framework on Cryogenian microbial facies, Rasthof Formation, Namibia. Geological Society London Special Publications 418, 170-175.

Le Ber, E., Le Heron, D.P., Winterleitner, G., Bosence, D.W.J., Vining, B.A., Kamona, F., 2013. Microbialite recovery in the aftermath of the Sturtian glaciation: Insights from the Rasthof Formation, Namibia. Sedimentary Geology 294, 1-12.

Li, C., Love, G.D., Lyons, T.W., Scott, C.T., Feng, L., Huang, J., Chang, H., Zhang, Q., Chu, X., 2012. Evidence for a redox stratified Cryogenian marine basin, Datangpo Formation, South China. Earth and Planetary Science Letters 331–332, 246-256.

Liu, P., Li, X., Chen, S., Lan, Z., Yang, B., Shang, X., Yin, C., 2015. New SIMS U–Pb zircon age and its constraint on the beginning of the Nantuo glaciation. Chinese Science Bulletin 60, 958-963.

Madejová, J., Komádel, P., 2001. Baseline Studies of the Clay Minerals Society Source Clays: Infrared Methods.

Mandernack, K., Post, J., Tebo, B., 1995. Manganese mineral formation by bacterial spores of the marine bacillus, Strain SG-1: Evidence for the direct oxidation of Mn (II) to Mn (IV). Geochimica et cosmochimica acta 59, 4393-4408.

Marshall, D.J. 1998. Cathodoluminescence of Geological Materials. Unwin Hyman, Boston, 146 pp.

Maynard, B., 2014. Manganiferous sediments, rocks, and ores, in: Holland, H.D., Turekian, K.K. (Eds.), Treatise of Geochemistry 2nd edition. Pergamon, Oxford, pp. 289-308.

Maynard, J.B., 2010. The Chemistry of Manganese Ores through Time: A Signal of Increasing Diversity of Earth-Surface Environments. Economic Geology 105, 535-552.

Müller, C.M., Pejcic, B., Esteban, L., Piane, C.D., Raven, M., Mizaikoff, B., 2014. Infrared Attenuated Total Reflectance Spectroscopy: An Innovative Strategy for Analyzing Mineral Components in Energy Relevant Systems. Scientific Reports 4, 6764.

Nealson, K.H., Tebo, B., Rosson, R.A., 1988. Occurrence and mechanisms of microbial oxidation of manganese. Adv. Appl. Microbiol. 33, 279-318.

Nealson, K.H. and Tebo, B., 1980. Structural features of Manganese precipitating Bacteria. Origins of Life, 10: 117-126.

Okolo, G.N., Neomagus, H.W.J.P., Everson, R.C., Roberts, M.J., Bunt, J.R., Sakurovs, R., Mathews, J.P., 2015. Chemical–structural properties of South African bituminous coals: Insights from wide angle XRD–carbon fraction analysis, ATR–FTIR, solid state 13C NMR, and HRTEM techniques. Fuel 158, 779-792.

Orange, D., Knittle, E., Farber, D. and Williams, Q., 1996. Raman spectroscopy of crude oils and hydrocarbon fluid inclusions: A feasibility study. The Geochemical Society, Special Publication, 5, pp.65-81.

Parikh, S.J., Chorover, J., 2006. ATR-FTIR spectroscopy reveals bond formation during bacterial adhesion to iron oxide. Langmuir 22, 8492-8500.

Pierrehumbert, R.T., Abbot, D.S., Voigt, A., Koll, D., 2011. Climate of the Neoproterozoic. Annual Review of Earth & Planetary Sciences 39, 417-460.

Polgári, M., Bajnóczi, B., Kis, K.V., Götze, J., Dobosi, G., Tóth, M., Vigh, T., 2007. Mineralogical and cathodoluminescence characteristics of Ca-rich kutnohorite from the Úrkút Mn-carbonate mineralization, Hungary. Min M 71, 493-508.

Polgári, M., Hein, J., Németh, T., Pál-Molnár, E., Vigh, T., 2013. Celadonite and smectite formation in the Úrkút Mn-carbonate ore deposit (Hungary). Sedimentary Geology 294, 157-163.

Polgári, M., Hein, J., Tóth, A., Pál-Molnár, E., Vigh, T., Bíró, L., Fintor, K., 2012b. Microbial action formed Jurassic Mn-carbonate ore deposit in only a few hundred years (Úrkút, Hungary). Geology 40, 903-906.

Polgári, M., Hein, J., Vigh, T., Szabó-Drubina, M., Fórizs, I., Bíró, L., Müller, A., Tóth, A., 2012a. Microbial processes and the origin of the Úrkút manganese deposit, Hungary. Ore Geology Reviews 47, 87-109.

Polgári, M., Hein, J.R., Bíró, L., Gyollai, I., Németh, T., Sajgó, C., Fekete, J., Schwark, L., Pál-Molnár, E., Hámor-Vidó, M., Vigh, T., 2016a. Mineral and chemostratigraphy of a Toarcian black shale hosting Mn-carbonate microbialites (Úrkút, Hungary). Palaeogeography, Palaeoclimatology, Palaeoecology 459, 99-120.

Polgári, M., Németh, T., Pál-Molnár, E., Futó, I., Vigh, T., Mojzsis, S.J., 2016b. Correlated chemostratigraphy of Mn-carbonate microbialites (Úrkút, Hungary). Gondwana Res 29, 278-289.

Pruss, S.B., Bosak, T., Macdonald, F.A., McLane, M., Hoffman, P.F., 2010. Microbial facies in a Sturtian cap carbonate, the Rasthof Formation, Otavi Group, northern Namibia. Precambrian Research 181, 187-198.

Rajabzadeh, M.A., Haddad, F., Polgári, M., Fintor, K., Walter, H., Molnár, Z., Gyollai, I., 2017. Investigation on the role of microorganisms in manganese mineralization from Abadeh-Tashk area, Fars Province, southwestern Iran by using petrographic and geochemical data. Ore Geology Reviews 80, 229-249.

Rosson, R.A. and Nealson, K.H., 1982. Manganese binding and oxydation by spores of a marine bacillus. J. Bacteriol., 151: 1027-1034.

Roy, S., 2006. Sedimentary manganese metallogenesis in response to the evolution of the Earth system. Earth-Science Reviews 77, 273-305.

Tang, S., Liu, T., 1999. Origin of the early Sinian Minle manganese deposit, Hunan Province, China. Ore Geology Reviews 15, 71-78.

Tang, Y., Zeiner, C.A., Santelli, C.M., Hansel, C.M., 2013. Fungal oxidative dissolution of the Mn(II)-bearing mineral rhodochrosite and the role of metabolites in manganese oxide formation. Environ Microbiol 15, 1063-1077.

Tebo, B.M., Bargar, J.R., Clement, B.G., Dick, G.J., Murray, K.J., Parker, D., Verity, R., Webb, S.M., 2004. Biogenic manganese oxides: properties and mechanisms of formation. Annu. Rev. Earth Planet. Sci. 32, 287-328.

Thamdrup, B., Rosselló-Mora, R., Amann, R., 2000. Microbial Manganese and Sulfate Reduction in Black Sea Shelf Sediments. Appl. Environ. Microbiol. 66, 2888-2897.

Wang, J., Li, Z.-X., 2003. History of Neoproterozoic rift basins in South China: implications for Rodinia break-up. Precambrian Research 122, 141-158.

Wang, T.-G., Li, M., Wang, C., Wang, G., Zhang, W., Shi, Q., Zhu, L., 2008. Organic molecular evidence in the Late Neoproterozoic Tillites for a palaeo-oceanic environment during the snowball Earth era in the Yangtze region, southern China. Precambrian Research 162, 317-326.

Webb, S.M., Dick, G.J., Bargar, J.R., Tebo, B.M., 2005. Evidence for the presence of Mn (III) intermediates in the bacterial oxidation of Mn (II). Proc. Natl. Acad. Sci. U. S. A. 102, 5558-5563.

Wu, C., Zhang, Z., Xiao, J., Fu, Y., Shao, S., Zheng, C., Yao, J., Xiao, C., 2016. Nanhuan manganese deposits within restricted basins of the southeastern Yangtze Platform, China: Constraints from geological and geochemical evidence. Ore Geology Reviews 75, 76-99.

Ye, Q., Tong, J., Xiao, S., Zhu, S., An, Z., Tian, L., Hu, J., 2015. The survival of benthic macroscopic phototrophs on a Neoproterozoic snowball Earth. Geology 43, 507-510.

Ye, Y., Wang, H., Zhai, L., Wang, X., Wu, C., Zhang, S., 2018. Contrasting Mo–U enrichments of the basal Datangpo Formation in South China: Implications for the Cryogenian interglacial ocean redox. Precambrian Research 315, 66-74.

Yee, N., Phoenix, V.R., Konhauser, K.O., Benning, L.G., Ferris, F.G., 2003. The effect of cyanobacteria on silica precipitation at neutral pH: implications for bacterial silicification in geothermal hot springs. Chemical Geology 199, 83-90.

Yin, L., 1990. Microbiota from Middle and Late Proterozoic Iron and Manganese Ore Deposits in China, in: Parnell, J., Ye Lianjun, Changming, C. (Eds.), Sediment-Hosted Mineral Deposits， Special Publications of International Association of Sedimentologists Blackwell Publishing Ltd., Beijing, pp. 109-117.

Yu, W., Algeo, T., Yuansheng, D., Maynard, B., Guo, H., Zhou, Q., Peng, T., Wang, P., Yuan, L., 2016. Genesis of Cryogenian Datangpo manganese deposit: Hydrothermal influence and episodic post-glacial ventilation of Nanhua Basin, South China. Palaeogeogr Palaeoclimatol Palaeoecol 459, 321–337.

Yu, W., Algeo, T.J., Du, Y., Zhou, Q., Wang, P., Xu, Y., Yuan, L., Pan, W., 2017. Newly discovered Sturtian cap carbonate in the Nanhua Basin, South China. Precambrian Research 293, 112-130.

Žák, L., Povondra, P., 1981. Kutnohorite from the Chvaletice pyrite and manganese deposit, east Bohemia. Tschermaks mineralogische und petrographische Mitteilungen 28, 55-63.

Zhang, F., Zhu, X., Yan, B., Kendall, B., Peng, X., Li, J., Algeo, T.J., Romaniello, S., 2015. Oxygenation of a Cryogenian ocean (Nanhua Basin, South China) revealed by pyrite Fe isotope compositions. Earth and Planetary Science Letters 429, 11-19.

Zhang, Q.-R., Li, X.-H., Feng, L.-J., Huang, J., Song, B., 2008a. A new age constraint on the onset of the Neoproterozoic glaciations in the Yangtze Platform, South China. The Journal of Geology 116, 423-429.

Zhang, S., Jiang, G., Han, Y., 2008b. The age of the Nantuo Formation and Nantuo glaciation in South China. Terra Nova 20, 289-294.

Zhou, C., Tucker, R., Xiao, S., Peng, Z., Yuan, X., Chen, Z., 2004. New constraints on the ages of Neoproterozoic glaciations in south China. Geology 32, 437-440.

Zhou, Q., Du, Y., Yuan, L., Zhang, S., Yu, W., Yang, S., Liu, Y., 2016. Rift Basin Structure and Its Control Function In Nanhua Period of Guizhou-Hunan-Chongqing Border Area. Journal of Earth Science 41, 177-188.

Figure and table captions

Fig. 1: (A) Tectonic map of China; (B) Paleogeographic map for the Cryogenian Nanhua Rift Basin, South China, rectangular outline shows the position of Fig. 2 A; (C) Cross-section for the post-Sturtian interglacial strata in the Nanhua Rift Basin.

Fig. 2: (A) Geological map for the Wuluo Village, Songtao County, Guizhou, South China; (B) Detailed geological map for the study area and locations of sampling sites.

Fig. 3: Lithologic columns and sampling locations for the mining tunnel section LB-A, LB-B and the drill core section ZK2001.

Fig. 4: The thin sections show mineralized biomats well visible on panorama photos of the respective samples (A) LB-171, (B) LB-304, (C) ZK2001-83, and (D) HU-LB-304; (E-F) display mineralized biomats under the optical microscope, PPL, sample HU LB-304; (G-H) illustrates mineralized biomats of sample HU LB-304 under the optical microscope, XPL; on (H) a rhythmic precipitation of silica is visible.

Fig. 5: The mineralized microbially produced micro-texture (MMPT) is a basic feature of all the samples. (A-B) sample LB-171 (optical microscope, PPL), filamentous, needle-like, spherical MMPTs are denoted by arrows, micron-size pyrite and amorphous organic materials can also be observed; (C) sample LB-304 (optical microscope, PPL), filamentous and spherical MMPTs are denoted by arrows; (D) sample HU-LB-304 (optical microscope, PPL), spherical and bead-like MMPTs are denoted by arrows.

Fig. 6: Optical microscope and cathodoluminescence photos of sample HU-LB-304. (A) optical microscope, PPL; (B) optical microscope, XPL; (C) optical microscope, PPL; (D) optical microscope, XPL; (E, F) CL image of the same part of Fig. 6 A B.

Fig. 7: EPMA-EDS back-scattered images of sample HU LB-304. (A) series of mineralized microbially produced micro-texture (MMPT); (B) enlargement of marked area in Fig. 7A; (C) framboidal pyrite; (D) micro-fossils preserved in the carbonate lamina; for composition see Table S2 and SI 1.

Fig. 8: (A) Thin section from rock sample HU-LB-304, with the line of Raman measurement (red line); (B-D) the number of peaks per 1 mm section; for legend see Table S3.

Fig. 9: Highest temperature calculation during the thermal evolution history of organic material based on Raman spectral analyses, using peak width (Raman carbonaceous material geothermometer, see Kouketsu et al. 2014).

Fig. 10: Simplified formation model of the microbial metallogenesis pathway for the Cryogenian DFMnD in Guizhou, South China.

Table 1. Sediment accumulation and rock formation hierarchy for the Cryogenian Datangpo Formation Mn ore deposits (bold text shows important aspects)

Table 2. Comparison of Cryogenian Datangpo Mn deposit in China and the Jurassic Úrkút Mn deposit in Hungary– differences.

Supporting Information

Microbial metallogenesis of the Cryogenian manganese ore deposits in South China

Wenchao Yu, Márta Polgári, Ildikó Gyollai, Krisztián Fintor, Máté Szabó, Ivett Kovács, József Fekete, Yuansheng Du, Qi Zhou*

SI 1. Measuring points on back scattered electron images, chemical and mineral composition (for details see Table 2) (EDS)

SI 2. Mineralogical distribution in Raman profiles (analysing points are in 10 μm interval).

SI 3. Peaks of minerals and mineralogical assemblages in the Raman profiles (analysing points are in 10 μm interval).

Table S1. Mineralogy based on FTIR-ATR for the Cryogenian Datangpo Foramtion manganese deposit in Guizhou, South China

Table S2. Chemical composition based on SEM-EDS measurements (wt.%) – (blue: kutnohorite; red: Ca-rhodochrosite)

Table S3. (A) Peak (lamina) numbers/mm sections and (B) lamina thickness calculation in sample HU-LB-304 in the Datangpo Formation manganese deposit of Guizhou, South China

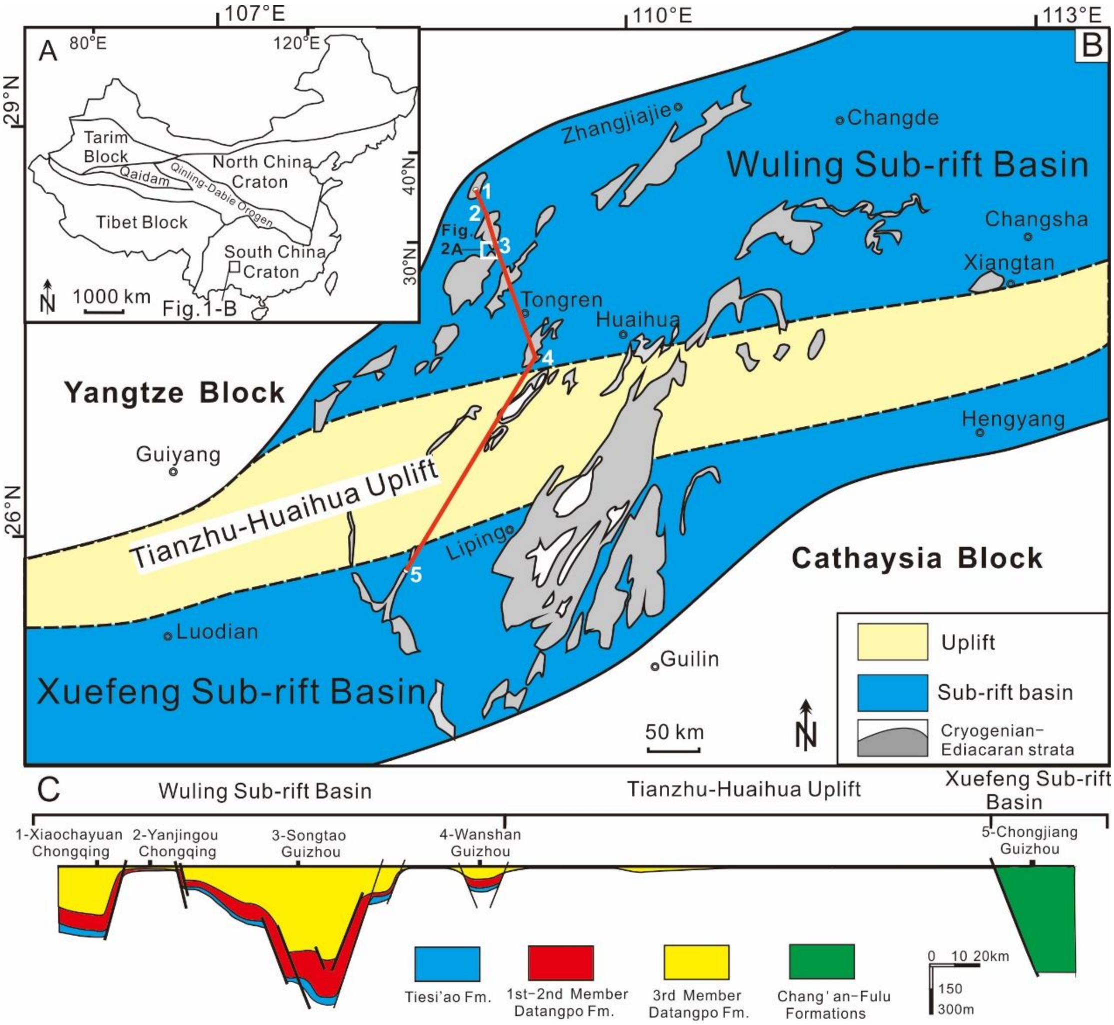

Fig. 1: (A) Tectonic map of China; (B) Paleogeographic map for the Cryogenian Nanhua Rift Basin, South China, rectangular outline shows the position of Fig. 2 A; (C) Cross-section for the post-Sturtian interglacial strata in the Nanhua Rift Basin.

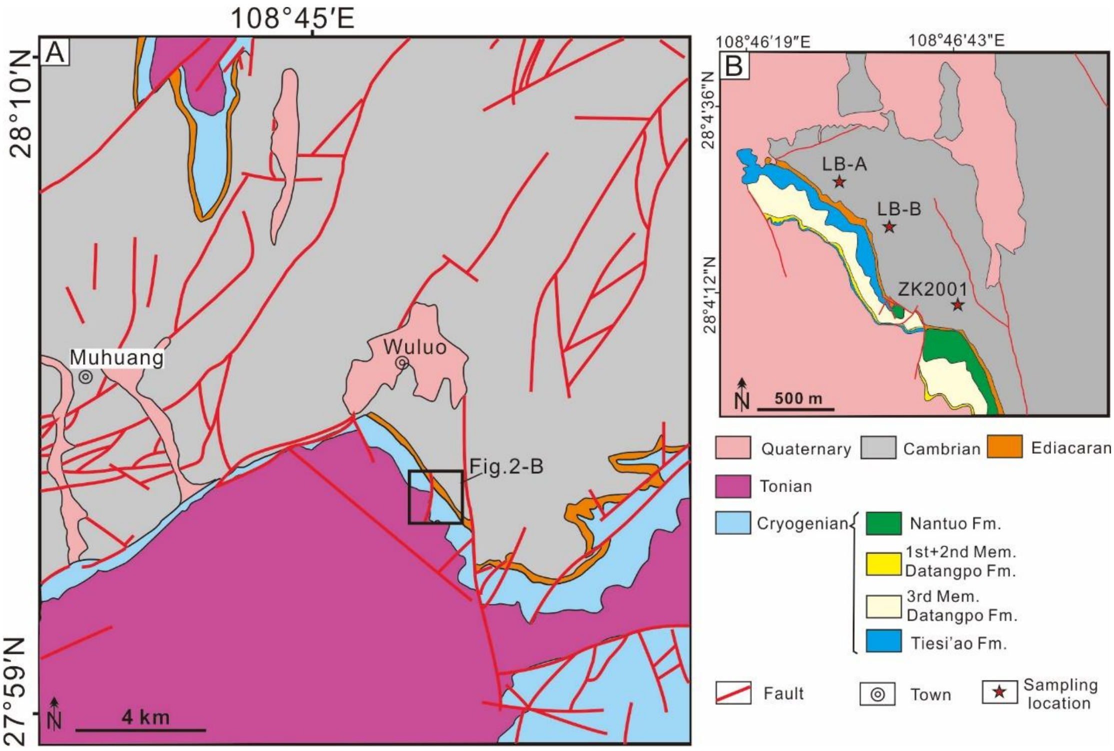

Fig. 2: (A) Geological map for the Wuluo Village, Songtao County, Guizhou, South China; (B) Detailed geological map for the study area and locations of sampling sites.

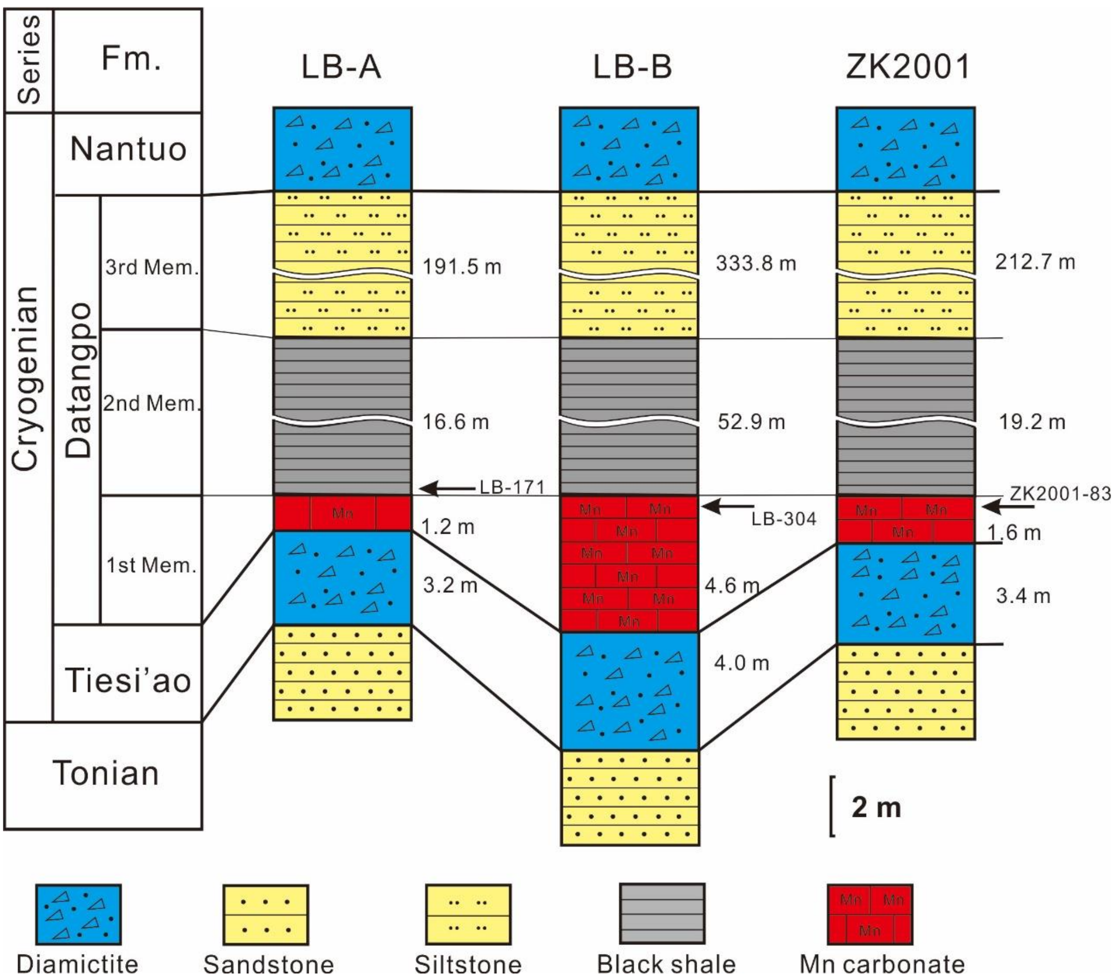

Fig. 3: Lithologic columns and sampling locations for the mining tunnel section LB-A, LB-B and the drill core section ZK2001.

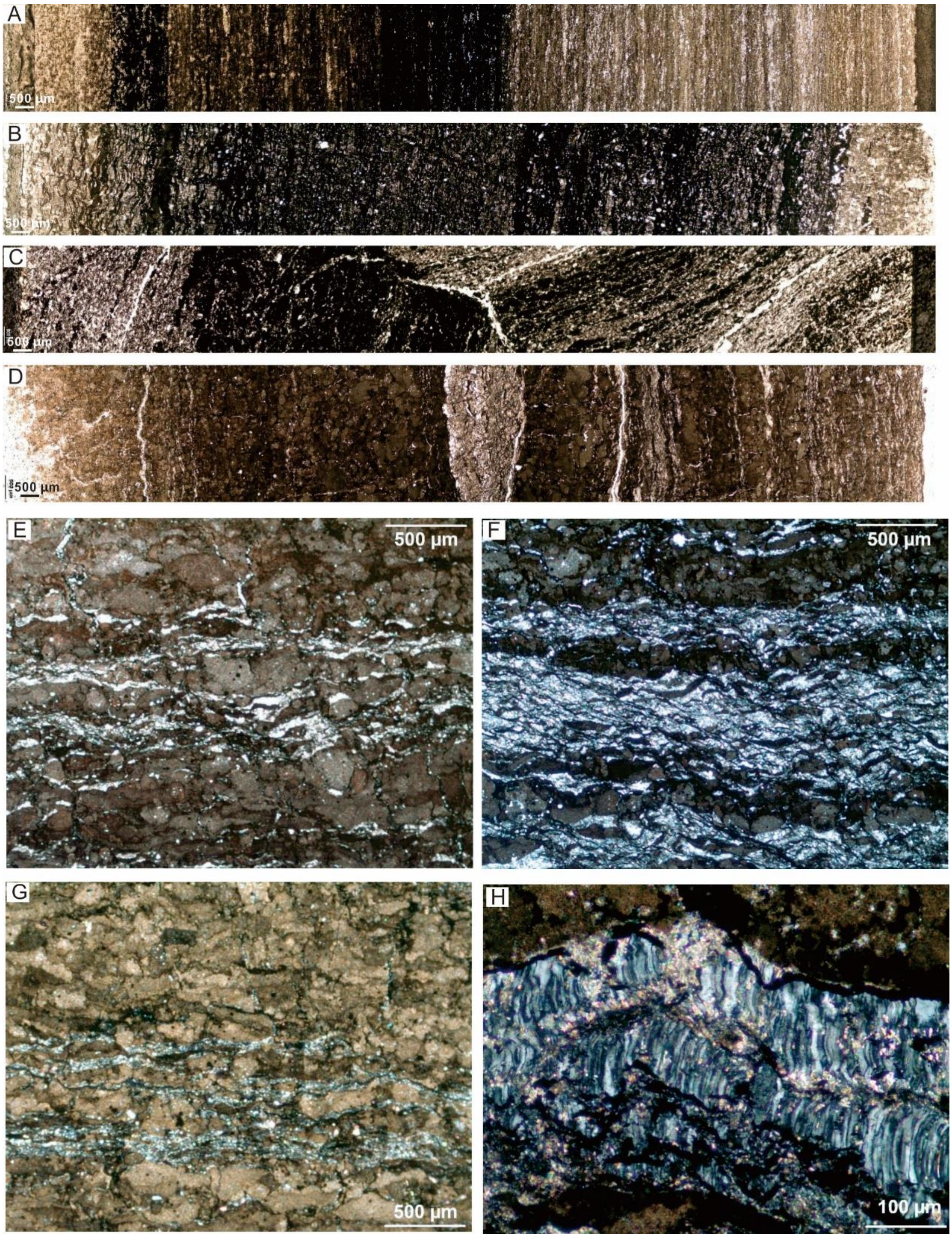

Fig. 4: The thin sections show mineralized biomats well visible on panorama photos of the respective samples (A) LB-171, (B) LB-304, (C) ZK2001-83, and (D) HU-LB-304; (E-F) display mineralized biomats under the optical microscope, PPL, sample

HU LB-304; (G-H) illustrates mineralized biomats of sample HU LB-304 under the optical microscope, XPL; on (H) a rhythmic precipitation of silica is visible.

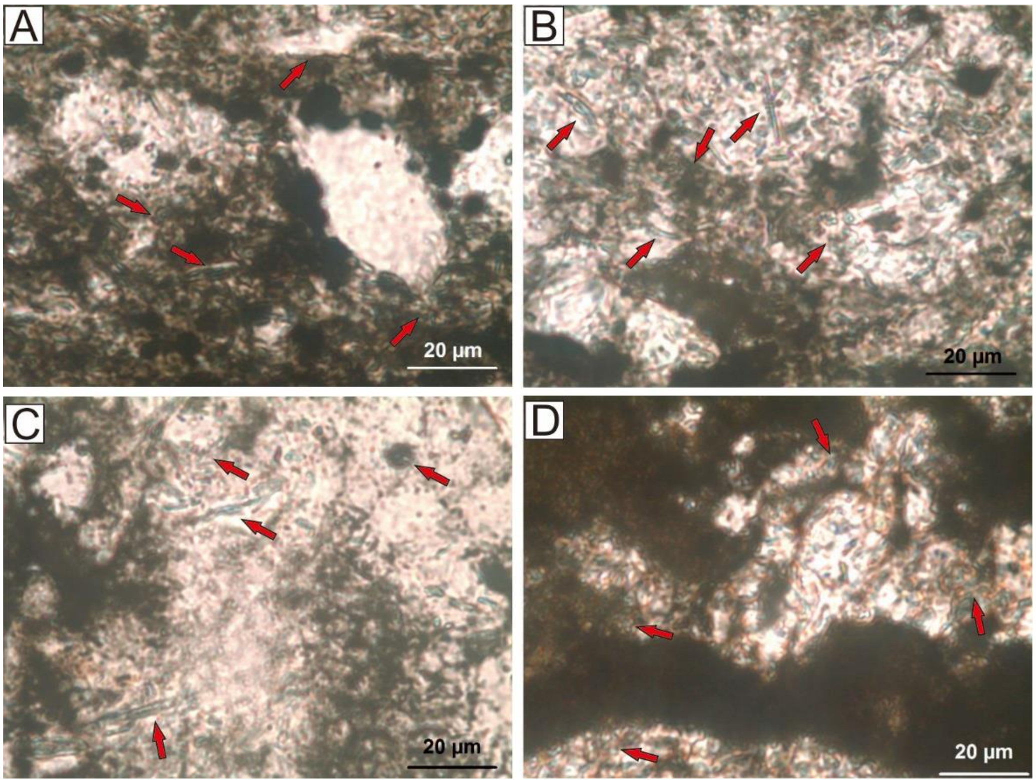

Fig. 5: The mineralized microbially produced micro-texture (MMPT) is a basic feature of all the samples. (A-B) sample LB-171 (optical microscope, PPL), filamentous, needle-like, spherical MMPTs are denoted by arrows, micron-size pyrite and amorphous organic materials can also be observed; (C) sample LB-304 (optical microscope, PPL), filamentous and spherical MMPTs are denoted by arrows; (D) sample HU-LB-304 (optical microscope, PPL), spherical and bead-like MMPTs are denoted by arrows.

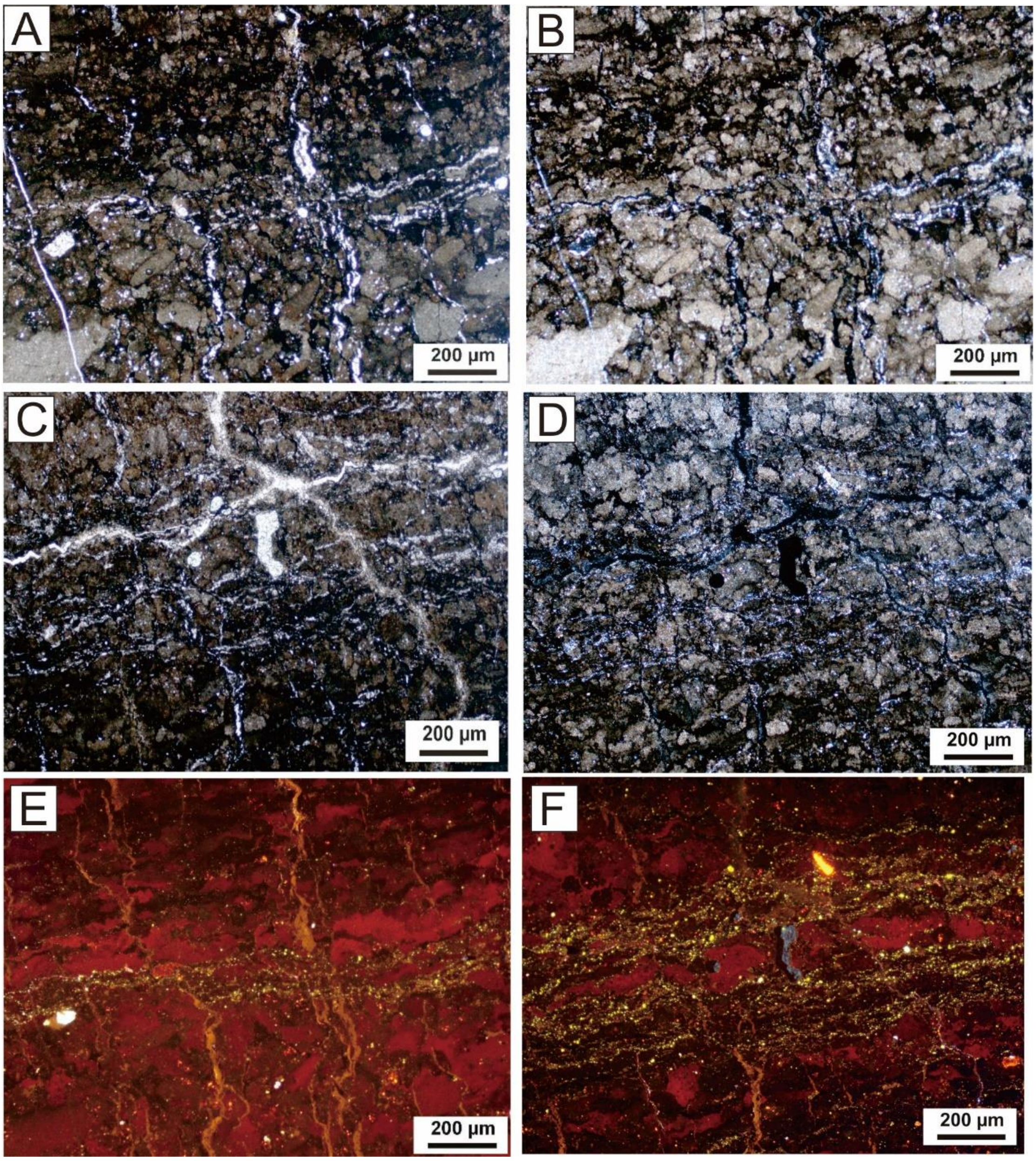

Fig. 6: Optical microscope and cathodoluminescence photos of sample HU-LB-304. (A) optical microscope, PPL; (B) optical microscope, XPL; (C) optical microscope, PPL; (D) optical microscope, XPL; (E, F) CL image of the same part of Fig. 6 A B.

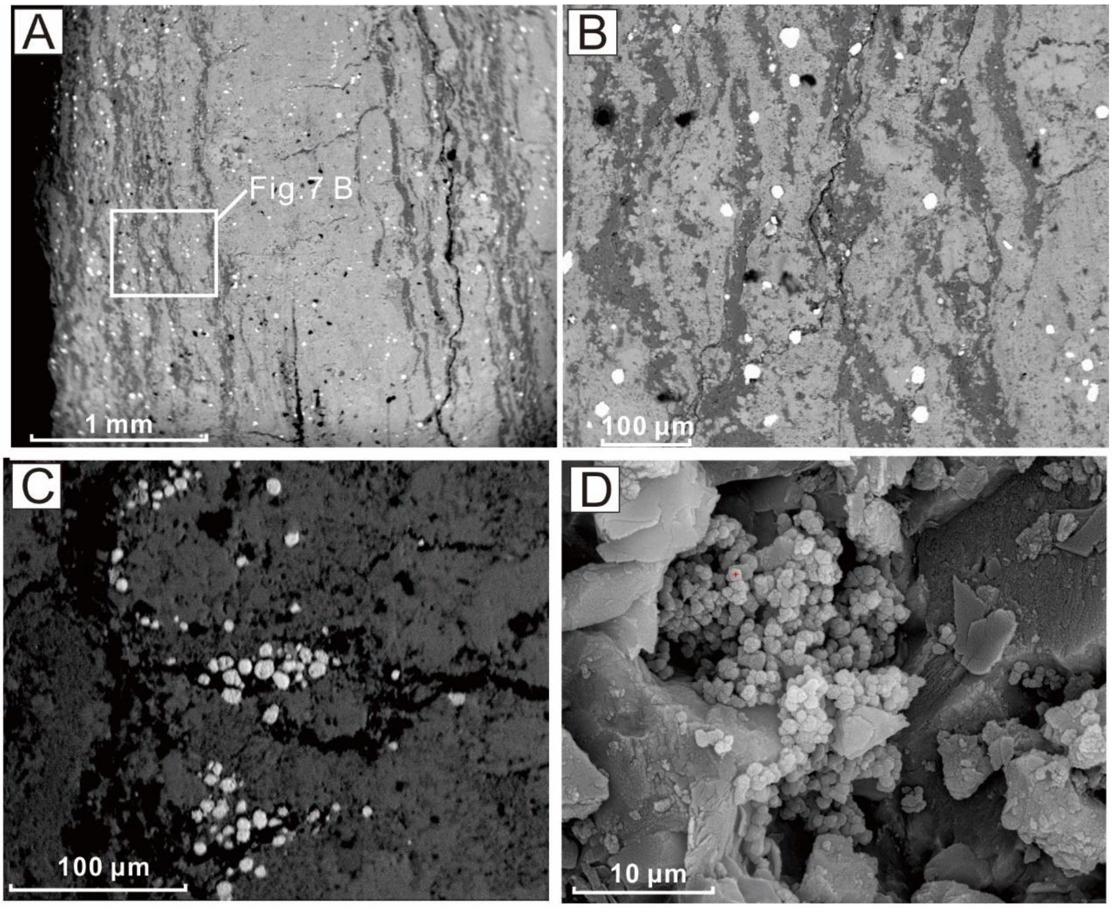

Fig. 7: EPMA-EDS back-scattered images of sample HU LB-304. (A) series of mineralized microbially produced micro-texture (MMPT); (B) enlargement of marked area in Fig. 7A; (C) framboidal pyrite; (D) micro-fossils preserved in the carbonate lamina; for composition see Table S2 and SI 1.

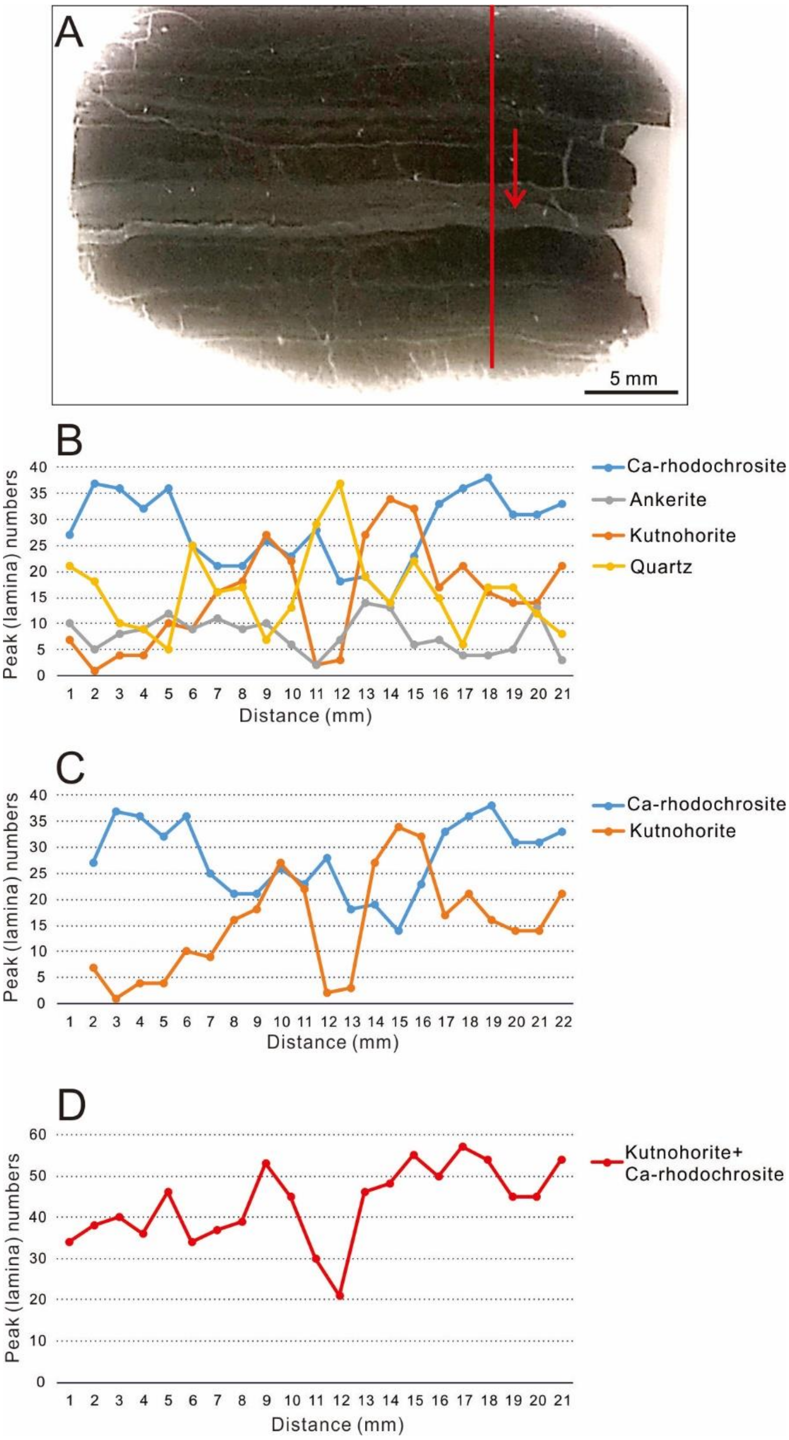

Fig. 8: (A) Thin section from rock sample HU-LB-304, with the line of Raman measurement (red line); (B-D) the number of peaks per 1 mm section; for legend see Table S3.

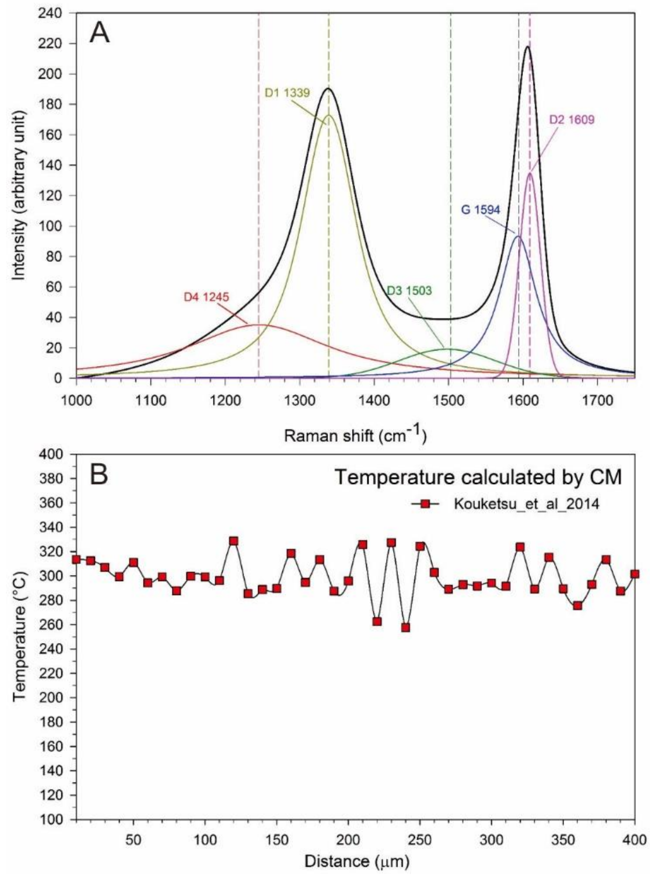

Fig. 9: Highest temperature calculation during the thermal evolution history of organic material based on Raman spectral analyses, using peak width (Raman carbonaceous material geothermometer, see Kouketsu et al. 2014).

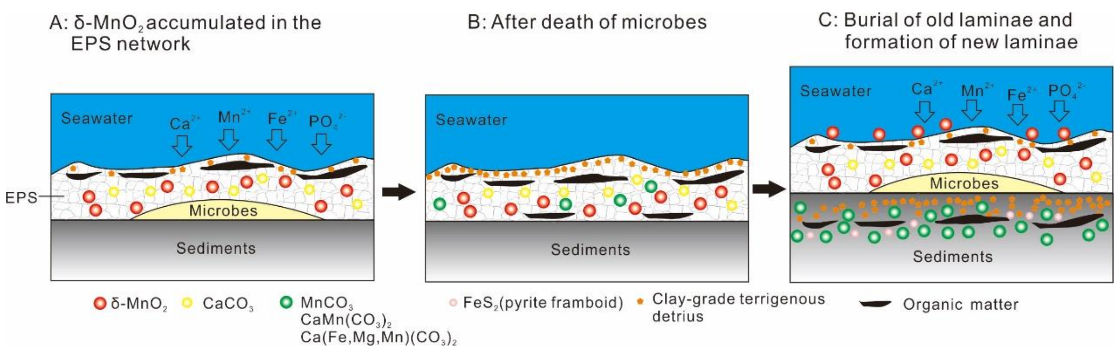

Fig. 10: Simplified formation model of the microbial metallogenesis pathway for the Cryogenian DFMnD in Guizhou, South China.